2015 ASIA-PACIFIC SOLAR RESEARCH CONFERENCE

Peer Reviewed
2015 Solar Research Conference

Madjid Sarvghad Moghaddam

Thermal Failure of a Nickel-base Superalloy Containing Carbonate Eutectic Salt

Madjid Sarvghad[1], Elaiza Luker[1], Stuart Bell[1], Ralf Raud[1], Theodore A. Steinberg[1] and Geoffrey Will[1]

[1]*Science and Engineering Faculty, Queensland University of Technology (QUT), Brisbane, Australia*

E-mail: madjid.sarvghadmoghaddam@hdr.qut.edu.au

Abstract

An Inconel 601 crucible containing a ternary eutectic mixture of lithium carbonate (Li_2CO_3), potassium carbonate (K_2CO_3) and sodium carbonate (Na_2CO_3) was placed into a 450˚C preheated furnace to check their compatibility as storage and containment materials for Thermal Energy Storage (TES) applications. Failure was observed after around 22 hours and proved to be assisted by the diffusion of oxygen and carbide forming elements through grain boundaries. Microstructural studies showed cracks of an intergranular type resulted from the high amount of residual stress and microstructural evolution during the thermal exposure; EBSD investigations confirmed the occurrence of partial recovery leading to stress reduction in the matrix. The failure of this nickel-based superalloy crucible was concluded to be a combination of stress induced by sensitization, exposure to hot corrosive media, and cold work manufacturing besides thermal instability of the microstructure.

1. Introduction

Thermal Energy Storage (TES) points to a new technology comprising of a storage medium, heat transfer mechanism and a containment material used in Concentrating Solar Thermal Power (CSTP) technologies (Kenisarin 2010, Gomez 2011, Bauer, Pfleger et al. 2013). TES systems normally consist of a containment material in the presence of a corrosive environment and thermal stresses (Leiby Jr and Ryan 1973, Rebak 2008, Rebak 2011, Bauer, Pfleger et al. 2013). Containment materials are usually made of carbon/stainless steels and nickel alloys. Nitrites, carbonates and fluorides are common candidates for storage mediums (Rebak 2008, Olson 2009, Olson, Ambrosek et al. 2009, Olson, Sridharan et al. 2010, Rebak 2011, Bauer, Pfleger et al. 2013, Sridharan and Allen 2013). The compatibility of the containment material with the storage medium and their stability during the repeated thermal cycling of a CSTP plant is a concerning issue in TES technologies (Kuravi, Trahan et al. 2013).

Inconel 601 (IN601/alloy 601) is a general-purpose structural engineering nickel-base alloy mostly used in heat and corrosion resistance applications owing to its high nickel and chromium content. The alloy comprises minor amounts of aluminum in the texture which enhances the oxidation resistance (Yu, Liaw et al. 2005) through the formation of a protective and adherent oxide film on the surface if exposed to high temperatures (Singh 2001).

However, the precipitation of continuous grain boundary (GB) carbides could endanger the corrosion resistance of Ni-base alloys at high temperatures. Previous studies show that

heating greatly sensitizes the material against intergranular corrosion (Gonzalez-Rodriguez and Fionova 1998, Hwang, Lim et al. 2013). Further investigation at 700˚C (Scarberry, Pearman et al. 1976) showed the precipitation of M_7C_3 carbides along GBs in Inconel 600. These carbides were mostly reported in lower Cr content alloys, unlike larger Cr content alloys in which $M_{23}C_6$ carbides are more common (Kai, Tsai et al. 1993, Wang and Gan 2001).

The presence of Ni_3Al intermetallic compound (IMC), which exhibits excellent characteristics at elevated temperatures (Ravindran, Subramoniam et al. 1996), and the penetration of oxygen through grain boundaries (Fournier, Delafosse et al. 2001, Pfaendtner and McMahon Jr 2001, Garat, Cloue et al. 2008) were reported to be other factors threatening these alloys at high temperatures.

The selection of appropriate and optimum structural material as a thermal energy vessel, subject to corrosive atmospheres and high temperatures, is essential in developing the economic and functional efficiency of a TES system. Therefore, this study aims to investigate the corrosion failure of Inconel 601 as a containment material for molten salts at high temperatures.

2. Experimental procedure

Two Inconel 601 crucibles with the chemical composition of (in wt%) 59.87% Ni, 21.75% Cr, 15.8% Fe, 1.55% Al, 0.32% Ti, 0.21% Mn, 0.13% Si, 0.08% Cu were used in this study. The as-received crucibles were products of Metal Technology, MTI Co manufactured via drawing to form the final product after cold rolling and solution annealing at 1150˚C.

A ternary carbonate eutectic mixture consisting of 32 wt% lithium carbonate (Li2CO3), 35% potassium carbonate (K2CO3) and 33% sodium carbonate (Na2CO3) was placed into one of the crucibles (approximately 1/5 full). The other crucible was used in as-received condition as the reference material (hereinafter referred to as reference sample-RS). The salt containing vessel was then placed into a 450˚C preheated furnace and initially checked at 1 hour intervals to ensure that rapid corrosion did not occur. During the first hours, the salt mixture remained relatively clear with no sign of rapid corrosion or deformation. After 22.75 hours, evident deformation occurred on the crucible and two cracks had initiated from the top, propagating downwards. After 25.25 hours, whilst the cracks continued to propagate downwards, the crucible (hereafter referred to as cracked sample-CS) was permanently removed from the furnace to ensure that the material does not undergo substantial damage prior to analysis.

2.1. Sample preparation

Suitable samples for SEM-EDS, EBSD and Optical Microscopy (OM) studies were selected from cut-off sections of both cracked and reference crucibles. Samples were mechanically wet polished down to 0.04 μm using colloidal silica, washed with ethanol and dried by hot air blow.

2.2. Microstructural investigation

2.2.1 Optical microscopy analysis

Microstructures were examined using an optical microscopy model Leica DM125 Stereo equipped with Leica Application Suite v4.5 software. An etchant comprising of 10gr CuSO4 + 50ml HCl + 50ml H_2O was then used for contrast enhancement in order to distinguish the discontinued areas of propagated cracks under optical microscopy.

2.2.2 Electron microscopy analysis

Microstructural changes were examined using a Field Emission SEM machine (model: JEOL 7001F, with automated feature detection equipped with secondary electron (SE) and EDS analysis system, OXFORD electron back-scatter diffraction (EBSD) pattern analyzer and Channel 5 analysis software).

Strain contouring component of OXFORD Channel 5 software was employed to estimate the extent of plastic deformation, or strain, in individual grains in EBSD maps. The Maximum Orientation Spread (MOS) map component was also used to highlight the degree of orientation change between every pixel in the grain and the grain's average orientation for each grain.

2.3. Corrosion investigation

Electrochemical experiments were conducted using three electrode cell containing the ternary carbonate eutectic mixture open to air at 450°C by using a VMP3-based BioLogic instrument controlled by EC-Lab® software. The tests were repeated at least three times and the results of reliable measurements without crevice problem were collected. Two platinum sheets as reference and counter electrodes were employed. Generalized corrosion test (GC) was conducted immediately after the immersion of both RS and CS cut-off samples at the potential scan rate of 10 mV/min and potential range of -250 to 250 mV with respect to Pt reference electrode finished in anodic region. It should be noted that, in order to study the very early effects of residual stress on the electrochemical properties, no open circuit potential test was carried out in which the elapsed time could reduce the amount of residual stress on samples.

3. Results and discussion

A micro-graph of the crack initiation and direction is shown in Figure.1a. This figure demonstrates that the crack has initiated from top and propagated towards the bottom of the crucible. Coarse elongated grains as a result of the drawing process point to the failure of recrystallization after around 25 hours of exposure to 450˚C. Figure.1b is a top-view macro-graph of the crucible sidewall which illustrates the crack growth direction across the crucible thickness. The serrated (inter-granular) morphology shows that the crack has first initiated from the outer diameter of the crucible and then propagated towards the inner diameter where, at its vicinity, the fracture toughness has reached its threshold value and failure continued with a brittle (trans-granular) morphology. Figure.2 provides a SEM fractography image to better illustrate the intergranularity of the crack morphology. Keeping in mind the last step in manufacturing process, drawing, such behaviour provides an evidence for the existence of maximum susceptibility at the outer diameter on top of the crucible where potentially the maximum amount of residual stress exists.

Elongated extra-coarse grains of single phase austenitic nickel (ɣ) with dispersed Ti-rich particles in the matrix form the overall microstructure as indicated in Figure.3a. For a clear comparison, strain contouring maps, IPF X colour maps and maximum orientation spread maps (MOS) of the same area as the band contrast image for both CS and RS specimens are depicted in Figures 3 and 4, respectively.

Figure.5 compares and contrasts deformation variations in the samples as strain distribution graphs corresponding to Figures.3b & 4b. The plot points to the relatively higher amount of plastic strain (and correspondingly greater residual stress) in RS as a result of drawing process. Figure.6 points to misorientation angle profiles inside two <111> directed grains corresponding to highlighted white lines in Figures.3c & 4c. CS represents a more

homogeneously oriented sub-grain structure rather than RS. It should be noted that the two peaks in RS profile point to twinnings inside the grain. Such comparisons highlight the occurrence of partial recovery in the matrix followed by the rearrangement of dislocations at the test temperature (Raabe 2014).

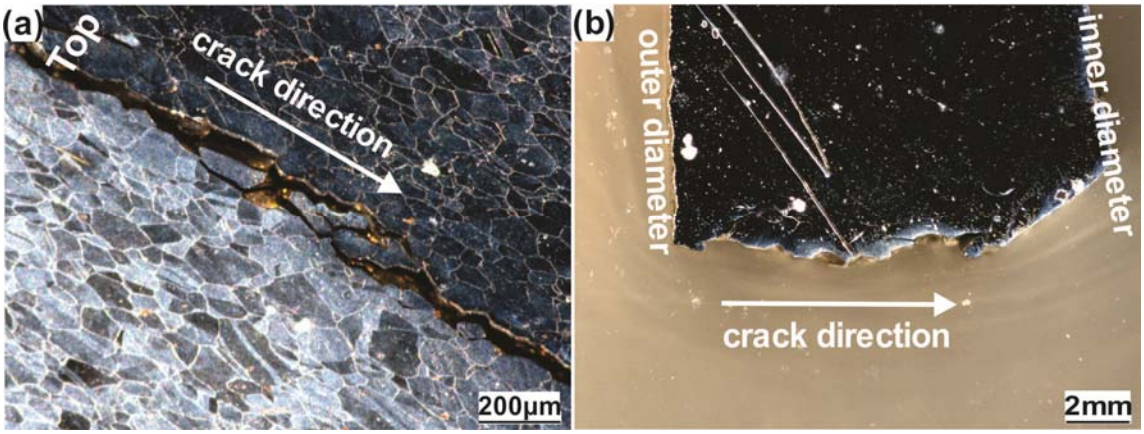

Figure 1. (a) Micro-graph image of the cracked crucible showing crack initiation area, top part of the crucible and growing direction downwards (etched sample), (b) top view macro-graph of the crucible sidewall showing outer and inner diameters and crack growth direction across the crucible wall (un-etched sample)

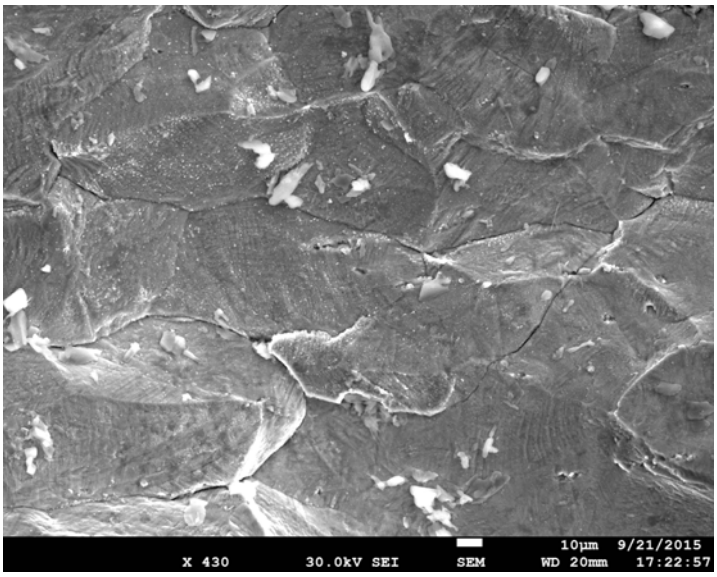

Figure 2. SEM-SE micrograph of the fracture surface showing 100% grain boundary crack morphology and salt residue

Finally, potentiodynamic curves illustrated in Figure.7 compare the electrochemical behaviour of samples in the eutectic molten salt at 450˚C. RS shows higher corrosion rate and more vulnerability to the corrosive media in the test condition. In other words, the early stages of the crucible exposure to molten salt involves higher corrosion rate which decreases as time elapses. This reduction accompanies by microstructural evolution due to the onset of partial recovery at the elevated temperature.

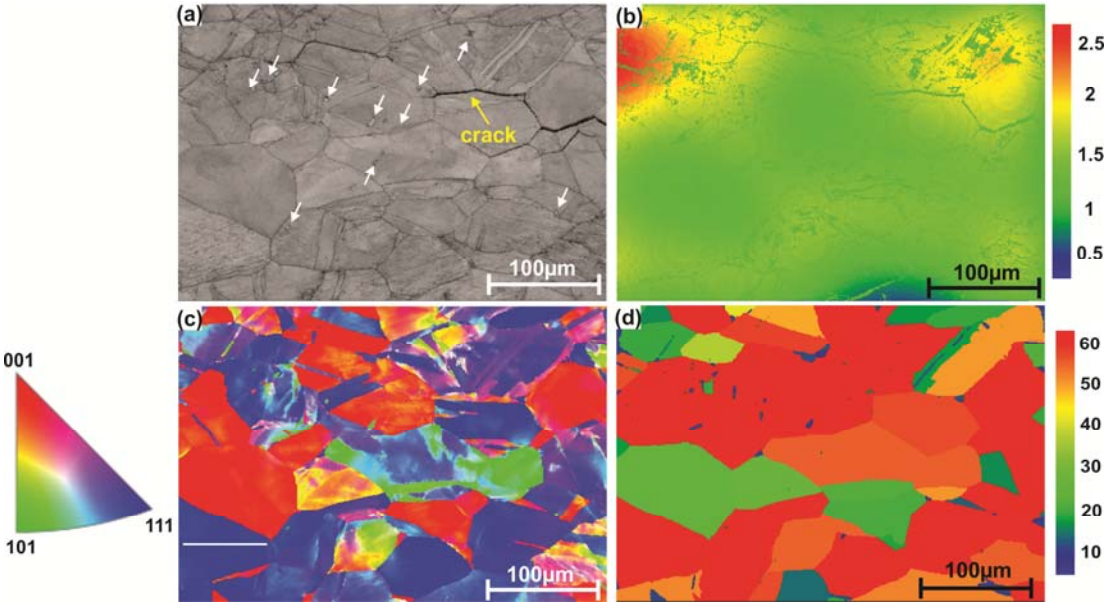

Figure 3. (a) Band contrast, (b) strain contouring map, (c) IPF X colour map, (d) maximum orientation spread map (MOS) of the same area in the cracked specimen (CS) including crack tip (yellow arrow). White arrows in (a) point to dispersed Ti-rich particles in the matrix; accelerating voltage= 25 kV, step size= 0.65 μm

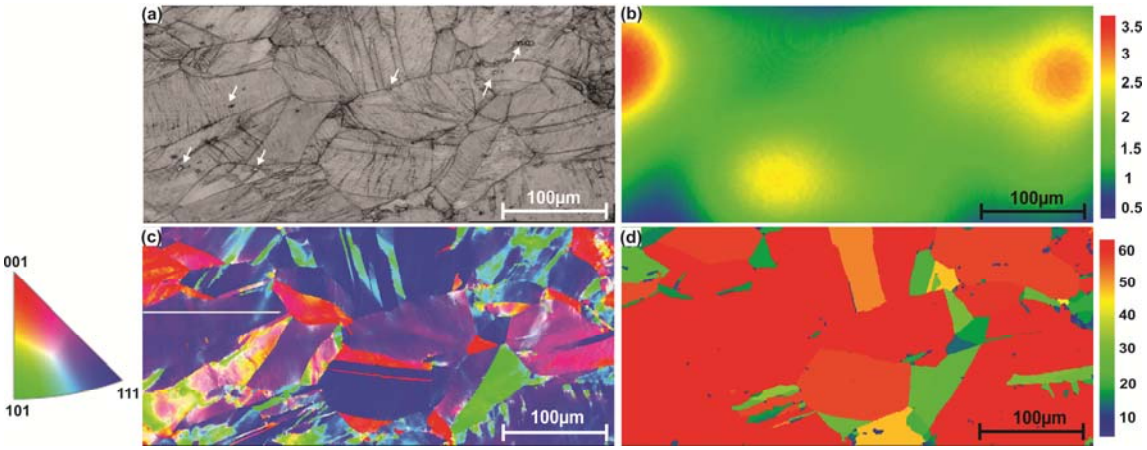

Figure 4. (a) Band contrast, (b) strain contouring map, (c) IPF X colour map, (d) maximum orientation spread map (MOS) of the same area in RS. White arrows in (a) point to dispersed Ti-rich particles in the matrix; accelerating voltage= 30 kV, step size= 0.5 μm

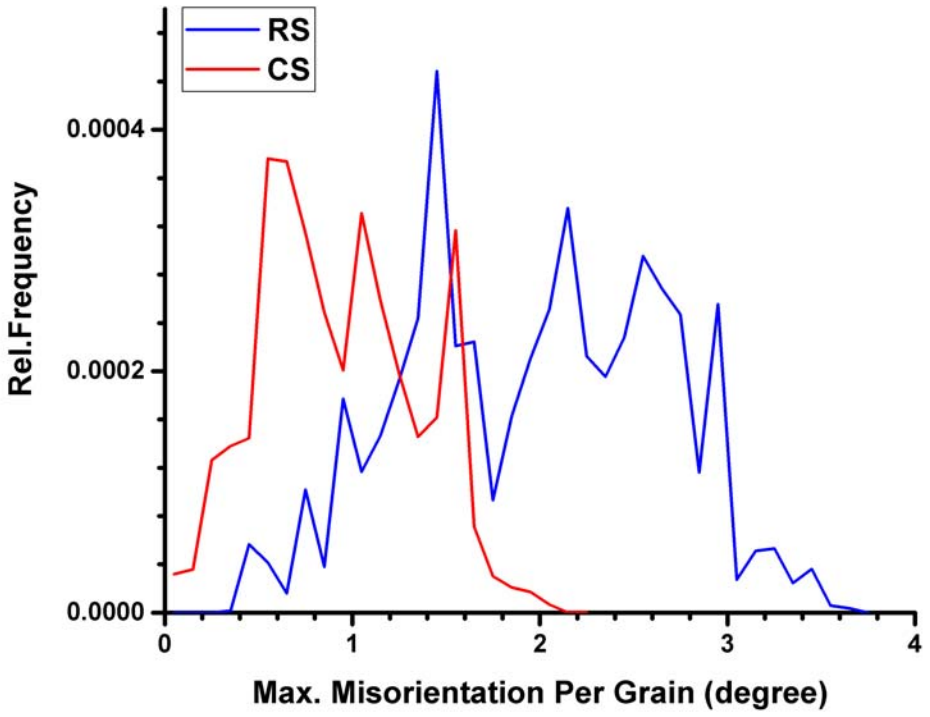

Figure 5. Strain contouring profile corresponding to maps in Figures.3b and 4b

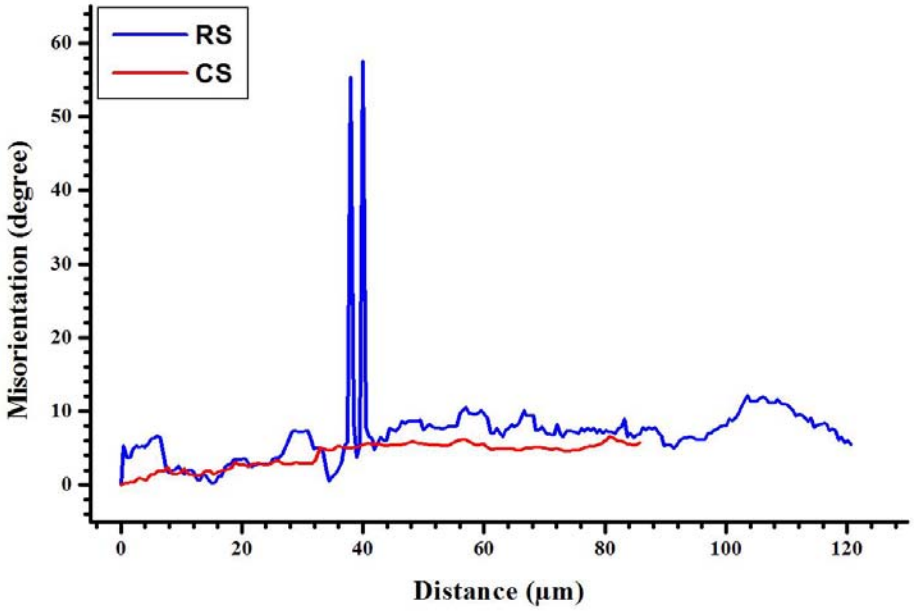

Figure 6. Misorientation distribution profile corresponding to [111] oriented grains highlighted by white lines in Figures. 3c and 4c

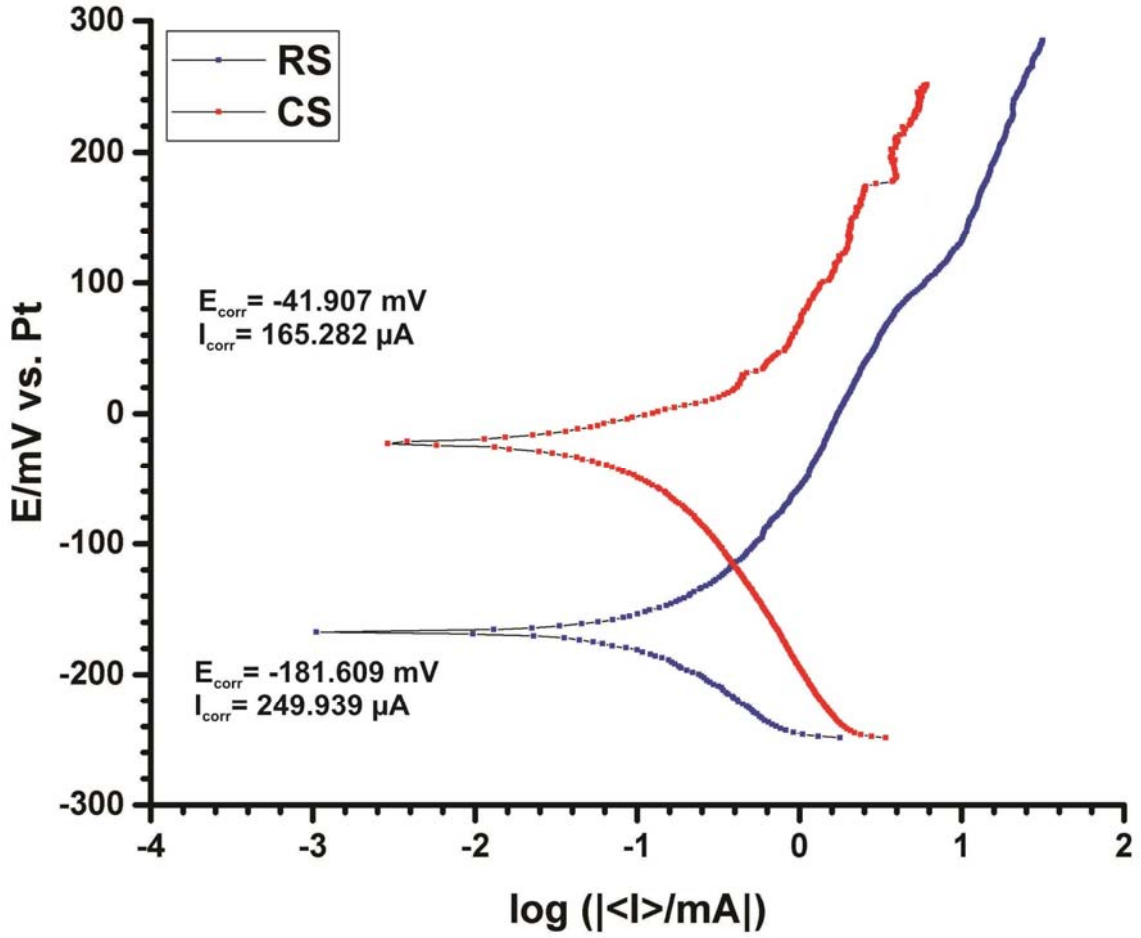

Figure 7. Potentiodynamic polarization curves comparing corrosion behaviour between RS and CS in the eutectic salt at 450˚C

Several factors could affect and dictate the crack initiation and propagation behaviour in the current study (Figures.1 & 2). The existence of dispersed Ti-rich particles in the matrix could lead to the formation of micro-galvanic cells as a result of Volta-potential difference between Ti and Ni in which Ti is more noble than nickel (McCafferty 2010). EBSD band contrasts show a random distribution of Ti in the matrix, i.e. it has dispersed randomly inside and between grains (at grain boundaries). This could be intensified by the formation of titanium carbides (TiC) at grain boundaries (Johnson and Stein 1974). The presence of Ni_3Al intermetallics (Ravindran, Subramoniam et al. 1996) and stress assisted GB oxidation followed by oxygen penetration through GBs at elevated temperatures (Pang, Dwyer et al. 1994) also lead to GB weakening. This could be also explained by the role of special boundaries in stress corrosion cracking (SCC) behaviour of Ni-base superalloys accompanied by oxygen-induced intergranular brittle fracture (Boehlert, Dickmann et al. 2006). Intergranular SCC followed by chromium depletion at GBs was also reported in Inconel 600 (Kikuchi, Takahashi et al. 2015) and proved to have a detrimental role in susceptibility to SCC by sensitizing GBs (Kai, Tsai et al. 1993).

However, the fact that the crack initiated from top outer side of the crucible (where it was not in direct contact with the molten salt) casts a shadow of doubt over the SCC nature of the crack. Although the potentiodynamic polarization curves show a meaningful tendency to

higher corrosion rates at the early stages of exposure, this tendency does not seem enough to initiate cracking. The SEM image in Figure.2 shows minor amounts of salt residue on the cracked side. This could be the salt penetrated through the crack after the propagation and does not necessarily point to failure as a result of exposure to molten salt. In other words, the corrosive media was not able to provide all the driving force needed for intergranular failure to initiate and only could act as a catalyst for GB weakening. In fact, the original cause of failure would be considered thermal sensitization as a result of microstructural evolution rather than a molten salt induced SCC.

The tendency to failure is expected to reduce with the elapse of time due to the strain reduction in CS as depicted by strain distribution and misorientation angle profiles (Figures 5 & 6). This reduction is accompanied by a known mechanism, recovery, in which dislocations with opposite strain fields meet and annihilate each other (Hrutkay 2013). This process comprises of a set of thermally activated microstructural reorganizations in the deformed material and leads to the release of stored internal energy (Raabe 2014). This energy release, in return, leads to more uniform corrosion behaviour with a lower rate, as shown in Figure.7. However, the energy release through the above process does not seem complete, as shown in strain distribution maps obtained from CS. The existence of residual stress in CS means that neither test temperature nor exposure time was high enough for a full recovery process to take place. On the other hand, the crack initiation time of 22.75 hours emphasises that a time consuming mechanism like diffusion should have controlled the failure. Therefore, the major factors determining the failure mechanism could be explained as microstructural evolution followed by partial recovery and GB sensitization. Long exposure time to elevated temperature provides driving force for the formation of oxides, carbides and/or Cr depletion at GBs through a diffusion controlled process. Finally, the simultaneous presence of residual stress, hot temperature, and diffusion of (O, Cr, Ti) leads to degradation via a GB failure mechanism. In this case, the term SCC could only account for the failure through oxidation in the presence of residual stress at GBs and does not seem relevant to the existence of the carbonate molten salt.

Based on the results above, it is suggested to apply atmosphere controlled equipment in order to prevent similar failure in CSTP plants that employ such combination of carbonate molten salts and superalloy containers.

4. Conclusion

The failure behaviour of a highly stressed Inconel 601 in a eutectic mixture of carbonate salt was studied by microstructural investigation and potentiodynamic polarization techniques. Results show that the residual stresses induced by the cold drawing process combined with corrosive hot ambient can raise the likelihood of localized oxidation. Thermal characteristics of test conditions provide driving force for intergranular failure through a sensitization mechanism. It involves the diffusion of oxide and carbide forming elements through grain boundaries followed by the presence of micro-galvanic cells as a result of Ti-rich precipitates in the matrix. A combination of the above makes GBs unprotected against failure.

References

Bauer, T., N. Pfleger, D. Laing, W.-D. Steinmann, M. Eck and S. Kaesche (2013). 20 - High-Temperature Molten Salts for Solar Power Application. Molten Salts Chemistry. F. L. Groult. Oxford, Elsevier**:** 415-438.

Boehlert, C. J., D. S. Dickmann and N. N. C. Eisinger (2006). "The effect of sheet processing on the microstructure, tensile, and creep behavior of INCONEL alloy 718." Metallurgical and Materials Transactions A **37**(1): 27-40.
Fournier, L., D. Delafosse and T. Magnin (2001). "Oxidation induced intergranular cracking and Portevin–Le Chatelier effect in nickel base superalloy 718." Materials Science and Engineering: A **316**(1-2): 166-173.
Garat, V., J. M. Cloue, D. Poquillon and E. Andrieu (2008). "Influence of Portevin–Le Chatelier effect on rupture mode of alloy 718 specimens." Journal of Nuclear Materials **375**(1): 95-101.
Gomez, J. (2011). High-Temperature Phase Change Materials (PCM) Candidates for Thermal Energy Storage (TES) Applications, National Renewable Energy Laboratory (NREL), Golden, CO.
Gonzalez-Rodriguez, J. G. and L. Fionova (1998). "The effect of structural evolution in INCONEL 601 on intergranular corrosion." Materials Chemistry and Physics **56**(1): 70-73.
Hrutkay, K. (2013). Evolution of Microstructure of Haynes 230 and Inconel 617 Under Mechanical Testing At High Temperatures Master's thesis, University of South Carolina.
Hwang, S. S., Y. S. Lim, S. W. Kim, D. J. Kim and H. P. Kim (2013). "ROLE OF GRAIN BOUNDARY CARBIDES IN CRACKING BEHAVIOR OF Ni BASE ALLOYS." Nuclear Engineering and Technology **45**(1): 73-80.
Johnson, W. C. and D. F. Stein (1974). "A study of grain boundary segregants in thermally embrittled maraging steel." Metallurgical Transactions **5**(3): 549-554.
Kai, J. J., C. H. Tsai and G. P. Yu (1993). "The IGSCC, sensitization, and microstructure study of Alloys 600 and 690." Nuclear Engineering and Design **144**(3): 449-457.
Kenisarin, M. M. (2010). "High-temperature phase change materials for thermal energy storage." Renewable & Sustainable Energy Reviews **14**(3): 955-970.
Kikuchi, H., H. Takahashi, H. Yanagiwara and T. Murakami (2015). "Relationship between ferromagnetic properties and grain size of Inconel alloy 600." Journal of Magnetism and Magnetic Materials **381**: 56-64.
Kuravi, S., J. Trahan, D. Y. Goswami, M. M. Rahman and E. K. Stefanakos (2013). "Thermal energy storage technologies and systems for concentrating solar power plants." Progress in Energy and Combustion Science **39**(4): 285-319.
Leiby Jr, C. C. and T. G. Ryan (1973). Thermophysical Properties of Thermal Energy Storage Materials-Aluminum, DTIC Document.
McCafferty, E. (2010). "Thermodynamics of Corrosion: Pourbaix Diagrams." 95-117.
Olson, L., K. Sridharan, M. Anderson and T. Allen (2010). "Intergranular corrosion of high temperature alloys in molten fluoride salts." Materials at High Temperatures **27**(2): 145-149.
Olson, L. C. (2009). Materials corrosion in molten LiF-NaF-KF eutectic salt, University of Wisconsin--Madison.
Olson, L. C., J. W. Ambrosek, K. Sridharan, M. H. Anderson and T. R. Allen (2009). "Materials corrosion in molten LiF–NaF–KF salt." Journal of Fluorine Chemistry **130**(1): 67-73.
Pang, X. J., D. J. Dwyer, M. Gao, P. Valerio and R. P. Wei (1994). "Surface enrichment and grain boundary segregation of niobium in inconel 718 single- and poly-crystals." Scripta Metallurgica et Materialia **31**(3): 345-350.
Pfaendtner, J. A. and C. J. McMahon Jr (2001). "Oxygen-induced intergranular cracking of a Ni-base alloy at elevated temperatures—an example of dynamic embrittlement." Acta Materialia **49**(16): 3369-3377.

Raabe, D. (2014). 23 - Recovery and Recrystallization: Phenomena, Physics, Models, Simulation. Physical Metallurgy (Fifth Edition). D. E. L. Hono. Oxford, Elsevier**:** 2291-2397.
Ravindran, P., G. Subramoniam and R. Asokamani (1996). "Ground-state properties and relative stability between the L 1 2 and DO a phases of Ni 3 Al by Nb substitution." Physical Review B **53**(3): 1129.
Rebak, R. B. (2008). Environmentally assisted cracking of nickel alloys —a review. Environment-Induced Cracking of Materials. S. A. S. H. J. M. O. B. Rebak. Amsterdam, Elsevier**:** 435-446.
Rebak, R. B. (2011). 7 - Stress corrosion cracking (SCC) of nickel-based alloys. Stress Corrosion Cracking. V. S. Raja and T. Shoji, Woodhead Publishing**:** 273-306.
Scarberry, R. C., S. C. Pearman and J. R. Crum (1976). "Precipitation Reactions in Inconel Alloy 600 and Their Effect on Corrosion Behavior." Corrosion **32**(10): 401-406.
Singh, I. B. (2001). "Pitting characteristics of alloy 600 and alloy 601 in a chloride-containing acidic environment." Corrosion **57**(6): 483-488.
Sridharan, K. and T. R. Allen (2013). 12 - Corrosion in Molten Salts. Molten Salts Chemistry. F. L. Groult. Oxford, Elsevier**:** 241-267.
Wang, J. D. and D. Gan (2001). "Effects of grain boundary carbides on the mechanical properties of Inconel 600." Materials Chemistry and Physics **70**(2): 124-128.
Yu, Y. K., D. W. Liaw and R. K. Shiue (2005). "Infrared brazing Inconel 601 and 422 stainless steel using the 70Au-22Ni-8Pd braze alloy." Journal of Materials Science **40**(13): 3445-3452.

Acknowledgements

This work is funded by the Australian Solar Thermal Research Initiative (ASTRI), which is supported by the Australian Government via the Australian Renewable Energy Agency (ARENA). The data reported in this paper were obtained at the Central Analytical Research Facility (CARF) operated by the Institute for Future Environments at Queensland University of Technology (QUT). Access to CARF was supported by generous funding from the Science and Engineering Faculty (QUT).